Basal conditions of Denman Glacier from glacier hydrology and ice dynamics modeling

Koi McArthur[1], Felicity S. McCormack[2], and Christine F. Dow[1,3]

[1]Department of Applied Mathematics, University of Waterloo, Waterloo, Canada
[2]Securing Antarctica's Environmental Future, School of Earth, Atmosphere & Environment, Monash University, Australia
[3]Department of Geography and Environmental Management, University of Waterloo, Waterloo, Canada

Correspondence: Koi McArthur (kr2mcarthur@uwaterloo.ca)

Abstract. Basal sliding in Antarctic glaciers is often modeled using a friction law that relates basal shear stresses to the effective pressure. As few ice sheet models are dynamically coupled to subglacial hydrology models, variability in subglacial hydrology associated with the effective pressure is often implicitly captured in the friction coefficient – an unknown parameter in the friction law. We investigate the impact of using effective pressures calculated from the Glacier Drainage System (GlaDS)

5 model on friction coefficients calculated using inverse methods in the Ice-sheet and Sea-level System Model (ISSM) at Denman Glacier, East Antarctica, for the Schoof and Budd friction laws. For the Schoof friction law, a positive correlation emerges between the GlaDS effective pressure and friction coefficient in regions of fast ice flow. Using GlaDS effective pressures generally leads to smoother friction coefficients and basal shear stresses, and smaller differences between the simulated and observed velocities, compared with using an effective pressure equal to the ice overburden pressure plus the gravitational

10 potential energy of the water. Compared with the Budd law, the Schoof law offers improved capabilities in capturing the spatial variations associated with known physics of the subglacial hydrology. Our results indicate that ice sheet model representation of basal sliding is more realistic when using direct outputs from a subglacial hydrology model, demonstrating the importance of coupling between ice sheet and subglacial hydrological systems. However, using our outputs we have also developed an empirical parameterization that improves application of the Schoof law without requiring explicit hydrological modeling.

15 ## 1 Introduction

The health of Antarctic glaciers and their future susceptibility to climate-driven change is often assessed by the retreat rates of their grounding lines and melt rates of adjacent ice shelves. In the East Antarctic, Denman Glacier (Fig. 1) has seen some of the fastest grounding line retreat of the last 20 years, losing 5.4 km since 1996 (Brancato et al., 2020), and the highest ice shelf melt rates of $116\,\mathrm{m\,a^{-1}}$ from 2010-2018 (Adusumilli et al., 2020). Perched on a grounding line above a deep trough that

20 descends 3.66 km below sea level (Morlighem et al., 2020), Denman is potentially at risk of marine ice sheet instability and rapid retreat, which is of significant concern given that the glacier drains a region containing 1.5 m of sea level equivalent.

Determining the future of Denman Glacier, and others in the Antarctic, largely relies on ice dynamics models to capture the evolution of ice flow under changing climates. These models frequently use inversion techniques to constrain important parameters that control ice velocity, including those related to the basal environment beneath the ice sheet (Morlighem et al.,
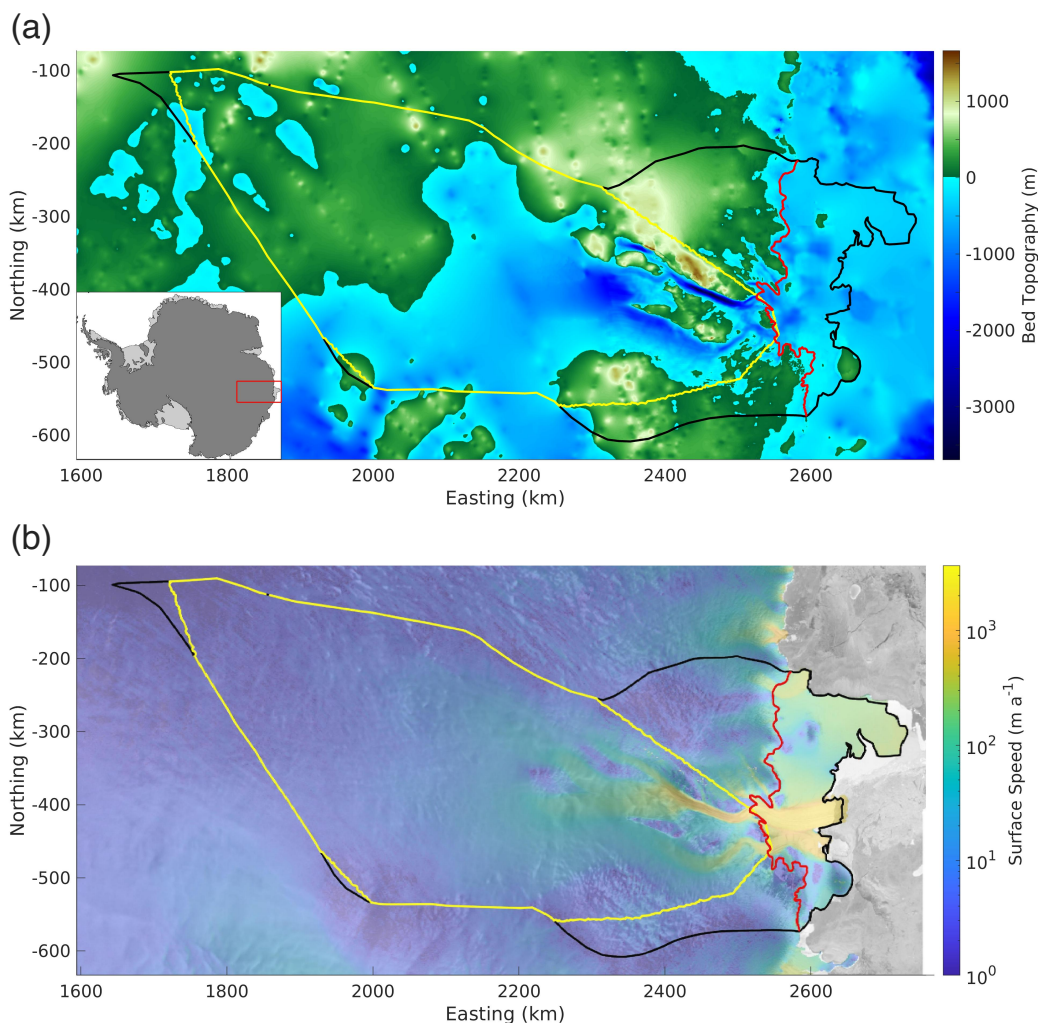
Figure 1. Denman-Scott catchment. **(a)** Bed elevation from Bechmachine v2 (Morlighem et al., 2020); **b** Surface speed (m a^{-1}) from MEaSUREs v2 (Rignot et al., 2011; Rignot, 2017), using a logarithmic color scale. The black lines in both panels show the catchment outline, defined by the drainage divide and calving front, the grounding line is shown in red, and the GlaDS domain in yellow. The $x-$ and $y-$axes are eastings and northings, defined in polar stereographic coordinates referenced to WGS84. These maps were made using the Antarctic Mapping Tools (Greene et al., 2017) and RAMP Radarsat Antarctic Mapping Project (Greene, 2022) toolboxes for MATLAB

25   2013). One such parameter is the basal friction coefficient, which is a key component of friction laws including the Weertman (1957), Budd et al. (1979) and Coulomb laws (Schoof, 2005; Gagliardini et al., 2007). Friction laws propose a functional dependency of the basal shear stress on the sliding velocity and in the case of the of the Budd and Coulomb laws, the effective pressure N, which is defined as the ice overburden pressure minus the water pressure. However, the dependency of the basal shear stress on other quantities, or unexpected dependency on sliding velocity and effective pressure, is implicitly captured in

30 the friction coefficient. Therefore, a spatially variable friction coefficient suggests a friction law which either fails to capture the proper functional dependency on sliding velocity and effective pressure, or omits the dependency of the basal shear stress on other quantities. Therefore, a friction coefficient that is both smooth – has little local variability – and has limited domain wide trends is desirable. In the search for ways of describing basal friction Beaud et al. (2022) propose a generalized friction law to be used on both rigid and deformable beds. They suggest that the unknown parameters in their friction law can be found

35 using surface velocity time series and inversion techniques on a variety glaciers implemented at the global scale.

Antarctic subglacial hydrology is increasingly being shown to be varied and dynamic, with large channels that discharge into ice shelf cavities (Dow et al., 2020; Indrigo et al., 2021), and effective pressures that vary spatially both above and below zero (i.e. the ice overburden pressure). Modeling of subglacial hydrology has shown close links between regions of low effective pressure and high ice surface velocity (Dow et al., 2018, 2020, 2022); this control of basal water pressure on sliding rates is

40 also well known for Greenland and Alpine glacier systems (Nienow et al., 2017; Iken and Bindschadler, 1986).

Despite the key role of basal boundary conditions, and in particular water pressure, on ice dynamics, there has not yet been a systematic investigation of the impact of the effective pressure on basal sliding in different friction laws applied in the Denman-Scott catchment. Given the critical role of the friction law for accurate ice dynamics and sea level predictions in the future (e.g. Åkesson et al., 2021; Yu et al., 2018), this is an important missing link. Here, we address this by using the Glacier

45 Drainage System (GlaDS; Werder et al., 2013) model to characterize the effective pressure and subglacial hydrology of the Denman Glacier. We use these effective pressures as inputs in the Budd and Schoof friction laws implemented in the Ice-sheet and Sea-level System Model (ISSM; Larour et al., 2012), and calculate the resulting basal friction coefficients using inversion.

2 Methods

2.1 GlaDS Setup

50 GlaDS is a 2D finite element subglacial hydrology model that calculates the development of a distributed water system on the elements, and channel growth, fed by the distributed system on the element edges (Werder et al., 2013). The model runs begin with no channels and therefore channel formation is dictated entirely by the evolving pressure and flow conditions across the model elements. GlaDS model equations are described in full in Werder et al. (2013) and its application to other Antarctic systems is covered in detail in Dow et al. (2018, 2020, 2022). The model parameters used in our simulations are summarized

55 in Table 1.

The domain for the GlaDS model is a subset of the grounded portion of the Denman-Scott catchment (Fig. 1). The mesh includes 17,700 nodes and the domain-wide mean edge length is 3.1 km. However, we refine the mesh to a minimum edge length of 200 m in regions where surface velocities are greater than 40 m a^{-1} and along the Denman Glacier grounding line. The basal and surface topography used in the GlaDS run is from BedMachine version 2 (Morlighem et al., 2020). Basal water

60 and sliding velocity inputs are computed from ISSM (Seroussi et al., 2019). The sliding velocity acts to open up distributed system cavities and, at velocities greater than 800 m a^{-1}, can cause model instabilities and so is capped at this value. We assume a temperate bed throughout, although regions with zero water input (in the interior or southernmost-regions of the

domain) are essentially frozen to the bed. The model is run for 10,000 days, providing outputs including channel size and discharge, distributed system discharge, water depth, and effective pressure.

Parameter	Value	Units
Bedrock bump height	0.08	m
Cavity spacing	2	m
Channel Conductivity	$5 \cdot 10^{-2}$	$\mathrm{m}^{3/2}{\cdot}\mathrm{kg}^{-1/2}$
Englacial void ratio	10^{-5}	
Glen's flow constant	3	
Ice density	910	$\mathrm{kg}{\cdot}\mathrm{m}^3$
Ice flow constant	$2.5 \cdot 10^{-25}$	$\mathrm{Pa}^3{\cdot}\mathrm{s}^{-1}$
Sheet conductivity	$1 \cdot 10^{-4}$	$\mathrm{m}^{7/4}{\cdot}\mathrm{kg}^{-1/2}$
Sheet Width Below Channel	2	m

Table 1. GlaDS model parameters.

2.2 ISSM Setup

ISSM is a finite-element model that uses an anisotropic mesh to simulate ice dynamics. We employ the inverse capabilities within ISSM to estimate basal friction coefficients in the Denman-Scott catchment using various friction laws, as described below. The inverse model uses the shallow-shelf approximation (SSA; MacAyeal, 1989) to the full Stokes equations, described in full in Larour et al. (2012).

The domain for the ISSM model is the full Denman-Scott catchment, extending the mesh used for the GlaDS simulations to include the floating ice shelves (Fig. 1). The ISSM mesh is comprised of 66,518 nodes, with anisotropic mesh refinement for faster flowing ice using the MEaSUREs v2 ice surface speed (Rignot et al., 2011; Rignot, 2017). The minimum mesh edge length is 500 m. We note that the GlaDS mesh used for the subglacial hydrology simulations differs from that used in the ISSM simulations for the ice dynamics as a result of differences in ice and hydrology drainage catchments; the impact of this is discussed in Appendix A. We test the sensitivity of the friction inversion simulations to various different meshes, finding that the results are less sensitive to the effect of the mesh configuration than to the specification of effective pressure and friction law used (Appendix B). The bed topography and surface elevation are from BedMachine v2 (Morlighem et al., 2020). The ice rigidity is calculated using inverse methods.

2.2.1 Solving for basal friction coefficients

We investigate the impact of the prescription of the effective pressure in the Budd and Schoof friction laws by calculating basal friction coefficients using inversion. The Budd friction law is given by the following expression:

$$\tau_b = \alpha^2 N u_b, \tag{1}$$

where τ_b (Pa) is the basal shear stress, α ($s^{1/2}\,m^{-1/2}$) is the friction coefficient, N (Pa) is the effective pressure and u_b ($m\,a^{-1}$) is the basal sliding speed. The Schoof friction law can be written as:

$$\tau_b = \frac{C^2 |u_b|^{m-1}}{\left(1 + (C^2/(C_{\max}N))^{1/m}|u_b|\right)^m} u_b, \tag{2}$$

where C ($kg^{1/2}\,m^{-2/3}\,s^{-5/6}$) is the friction coefficient, m is the power law exponent, here given by $m = 1/3$, and $C_{\max}$ ($m^{-1/3}\,s^{1/3}$) is Iken's bound, which is the effective cap on the basal shear stress.

For each friction law, we calculate inversion for the basal friction coefficients by minimizing a cost function that includes the contributions of absolute and logarithmic misfits between the observed and simulated ice speeds (Morlighem et al., 2013). Weighting parameters for the absolute and logarithmic misfit terms for the various friction laws are shown in Table C1. We also add a Tikhonov regularization term to the cost function, which regulates the local variability in the friction coefficient by penalizing large gradients in the friction coefficient, making the friction coefficient smoother. The weighting parameter of the Tikhonov regularization term is determined using an L-curve analysis (Appendix C; Hansen, 2000) which allows us to find a friction coefficient with small local variability while maintaining a good absolute and logarithmic velocity misfit. The final weighting parameters for the Tikhonov regularization term for each friction law are reported in Table C1.

We compare the difference in the friction coefficients when we use two different prescriptions for the effective pressure: (1) an effective pressure given by assuming water pressure equals the ice overburden pressure plus the gravitational potential energy of the water $N = \rho_i g H + \rho_w g B$, which we refer to as N_O; and (2) the effective pressure taken directly from the GlaDS simulations, which we refer to as N_G. We cap the effective pressure at 1 % of ice overburden pressure for Budd runs and 0.4 % of ice overburden pressure for Schoof runs, due to numerical artefacting that arises for values smaller than this. The impact of these choice of caps is discussed in Appendix D.

3 Results

We present the results of the GlaDS modeling followed by the inversion results using ISSM, and compare the impact of using the GlaDS effective pressure outputs with those using N_O for the Schoof and Budd friction laws.

3.1 Subglacial hydrology

Major subglacial hydrology channels form in the Denman-Scott catchment, with significant discharge through both the Denman (Fig. 2a (i)) and Scott Glaciers (Fig. 2a (ii)). For the former, the discharge is $15.8\,m^3\,s^{-1}$ and for the latter, $6.0\,m^3\,s^{-1}$. The Denman channel initiates as two branches that flow for 80 and 52 km through subglacial valleys before merging at the beginning of the significantly overdeepened trough. From here, the channel flows through the base of the trough, emerging 129 km downstream at the grounding line. The Scott channel, on the other hand, converges as a single channel 95 km from the grounding line. There is substantial water amalgamation with a maximum depth of 25 m in a basal depression (Fig. 2d (v)) that feeds the channels of both the Denman and Scott Glaciers, although with the strongest flux towards Denman (Fig. 2a). The bed topography of this basin feature lies at 1900 m below sea level (Fig. 1a), and subglacial water flows upslope by approximately
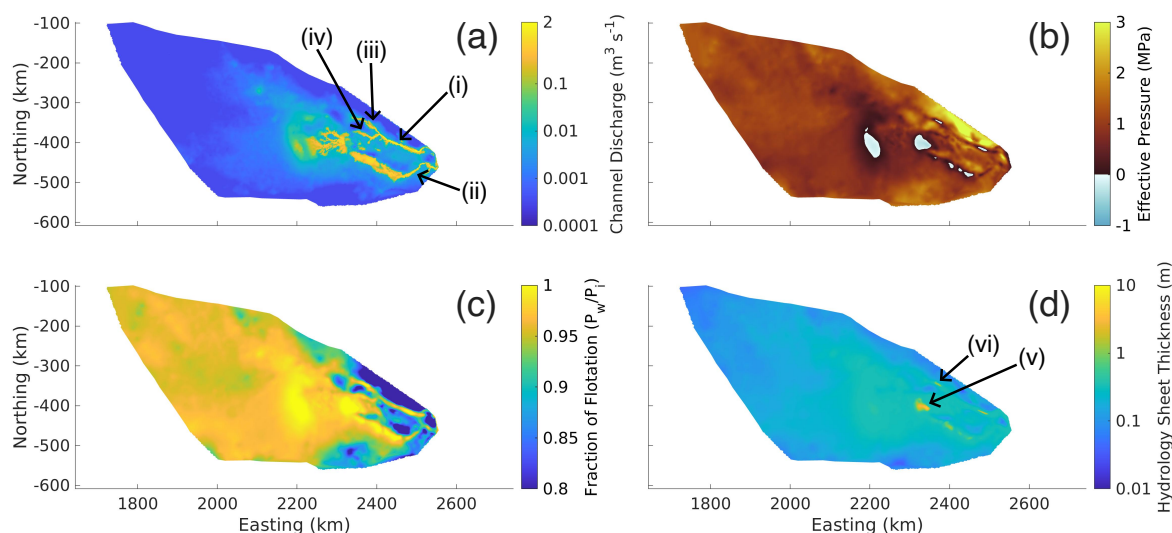
Figure 2. GlaDS simulation results. **(a)** Channel discharge ($m^3\,s^{-1}$); **(b)** effective pressure (MPa); **(c)** fraction of flotation (i.e. the fraction of overburden pressure that each grid cell is pressurized to); and **(d)** water sheet thickness (m). The locations marked in panel **(a)** are the: **(i)** Denman channel; **(ii)** Scott channel; **(iii)** western branch of the Denman channel; **(iv)** eastern branch of the Denman channel. The locations marked in panel **(d)** are the: **(v)** basin like feature; and **(vi)** lake like feature.

1200 m to drain downstream. A second 'lake-like' feature feeds the northern branch of the Denman channel and reaches a

115 water depth of ∼8 m (Fig. 2d (vi)).

As effective pressure is the ice overburden pressure minus the water pressure, low effective pressure implies high water pressure, with negative effective pressure implying that the water pressure is greater than the ice overburden pressure. A low effective pressure corresponds to a high fraction of flotation which is defined to be the water pressure divided by the ice overburden pressure. When the water pressure is equal to the ice overburden pressure flotation is reached and the fraction of

120 flotation is 100 %. Effective pressure in the GlaDS outputs is lowest in the basin feature and the lake-like feature, reaching -0.4 MPa in the former and -0.25 MPa in the latter (Fig. 2b). This translates to a maximum of 101 % fraction of flotation relative to the ice overburden pressure for both sites (Fig. 2c). Other regions of negative effective pressure occur in the troughs of Denman and Scott Glaciers. Low effective pressures, close to zero (>92 % fraction of flotation), persist through the upper regions of the domain and through the subglacial valleys and troughs of both glaciers. Close to the grounding line, effective

125 pressures rise to 90 % fraction of flotation in the regions where the channels of both glaciers exit into the ice shelf cavity.
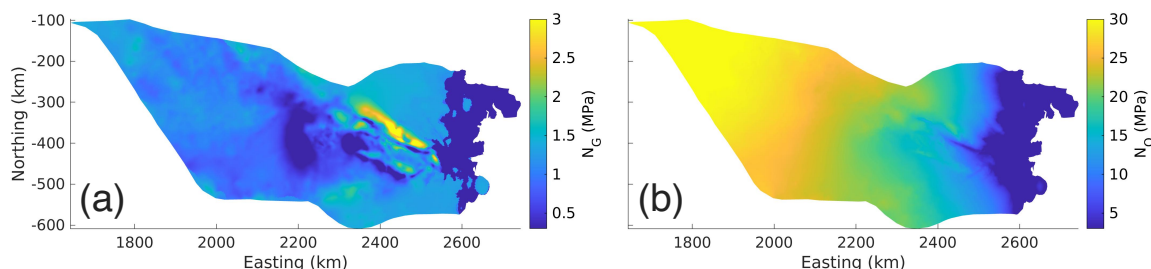
Figure 3. Effective pressure inputs. **(a)** N_G, capped at 0.4% overburden for the Schoof friction law shown here; **(b)** prescribed effective pressure equal to the ice overburden pressure plus the gravitational potential energy of water $N_O = \rho_i gH + \rho_w gB$.

3.2   Ice dynamics and inversion

We first consider the results for the Schoof friction law. When using the GlaDS effective pressures (N_G; Fig. 3a), the Schoof friction coefficient estimated using inversion is relatively uniform across the basin, with over 50 % of the basin recording friction coefficients that range between 2910 and 3580 $\text{kg}^{1/2}\,\text{m}^{-2/3}\,\text{s}^{-5/6}$ (Fig. 4a). Departures from this occur in isolated

130 patches of very low and very high friction – corresponding to the lake-like feature feeding the northern branch of the Denman channel – and a region directly upstream of this feature where the ice surface speeds abruptly decrease. The friction coefficients are relatively lower in the Denman and Scott troughs, and alternating high and low "stripes" are evident in the region of slow flow (ice surface speeds $<50\,\text{m\,a}^{-1}$) to the west of the Denman Glacier and south of the Shackleton Ice Shelf (we note that this region was excluded from the GlaDS model; see discussion in Appendix A).

135 The Schoof friction coefficient estimated using N_G is smoother compared with that using N_O (Fig. 4a and Fig.4c; Appendix C). Here, a smoother friction coefficient resulted in lower median and mean differences and root mean square errors (rmse) between the simulated and observed surface speeds for the N_G simulation over the N_O simulation (Table 2; Fig. 4b,d), particularly in regions of faster flow (surface speeds $>10\,\text{m\,a}^{-1}$). We find a positive correlation between N_G and the friction coefficient (correlation coefficient $r^2 = 0.30$; Fig. 5a), and the relationship is stronger when we exclude regions of slow flow

140 (surface speeds $<10\,\text{m\,a}^{-1}$), where the effective pressure and friction coefficient are lowest. By contrast, there is only a slight positive correlation between N_O and friction coefficient ($r^2 = 0.15$) when using the Schoof friction law.
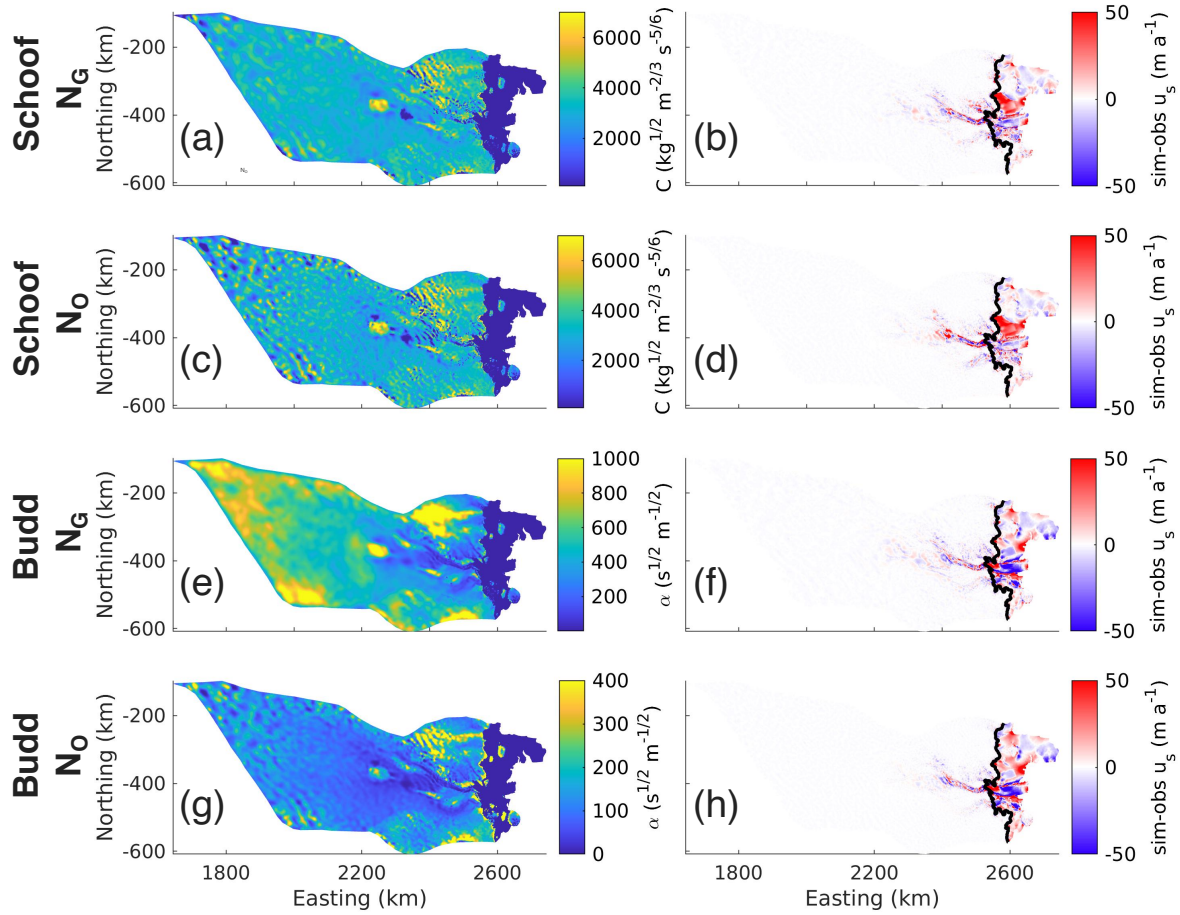
Figure 4. Ice dynamics outputs. **(a)**, **(c)**, **(e)**, **(g)** are friction coefficients, **(b)**, **(d)**, **(f)**, **(h)** is the difference between the simulated and observed velocity ($\mathrm{m\,a^{-1}}$). **(a)** and **(b)** show outputs from the Schoof law with N_G; **(c)** and **(d)** are from the Schoof law with N_O; **(e)** and **(f)** are from the Budd law with N_G; and **(g)** and **(h)** are from the Budd law with N_O.

Friction Law	Effective Pressure	difference between simulated and observed surface speeds		
		median ($\mathrm{m\,a^{-1}}$)	**mean** ($\mathrm{m\,a^{-1}}$)	**root mean square error** ($\mathrm{m\,a^{-1}}$)
Schoof	N_G	0.185	0.607	10.1
	N_O	0.226	0.799	11.3
Budd	N_G	0.0847	-0.0700	11.5
	N_O	0.265	0.265	11.7

Table 2. Median, mean, and root mean square error (rmse) of the differences between the simulated and observed ice surface speeds for the Schoof and the Budd friction laws using the GlaDs effective pressure (N_G) or an effective pressure equal to overburden pressure plus the gravitational potential energy of water (N_O).
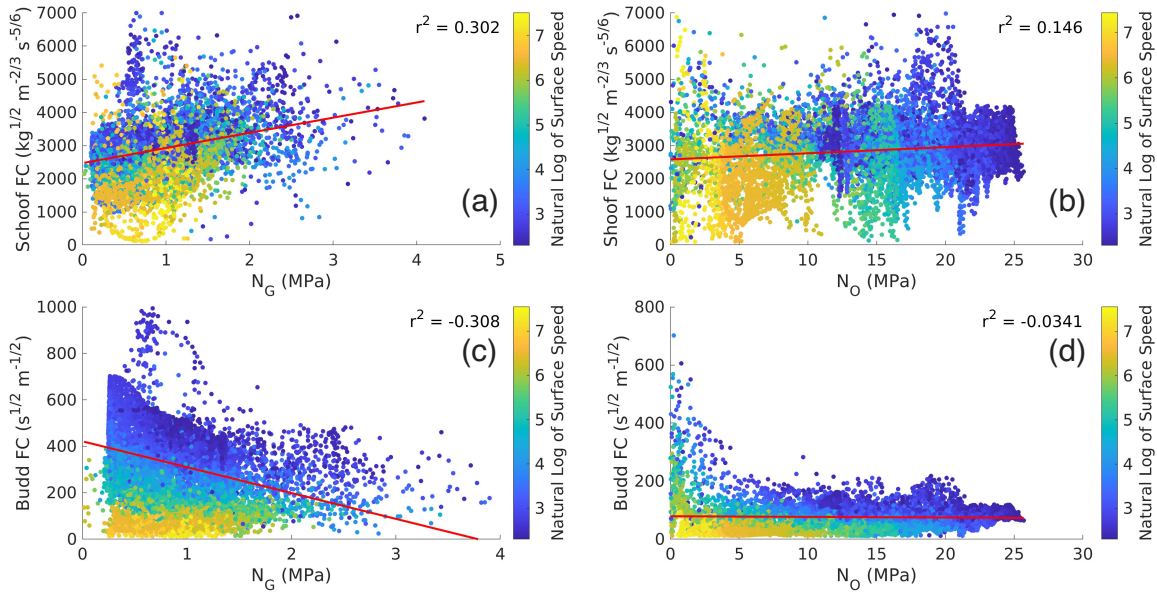
Figure 5. Relationship between the effective pressure and friction coefficient for: **(a)** Schoof friction coefficient with N_G; **(b)** Schoof friction coefficient with N_O; **(c)** Budd friction coefficient with N_G; and **(d)** Budd friction coefficient with N_O. In each panel, points are colored by the natural log of the surface speed. The red line is the linear line of best fit, and the slope of this line is reported.

We next compare the difference between friction coefficients with the Schoof and Budd friction laws and using N_G. All friction coefficients are relatively lower in the Denman and Scott Glacier troughs and the lake-like and basin features that feed into these troughs, and relatively higher in the region between the lake-like and basin features (Fig. 4a,c,e,g). However,
145   the range of the friction coefficient across the catchment estimated with the Budd friction law is substantially greater than that with the Schoof friction law, with relatively high values in the interior of the catchment compared with towards the coast. This leads to a comparatively greater standard deviation in the Budd friction coefficient compared with that of Schoof ($1240\,\mathrm{kg}^{1/2}\,\mathrm{m}^{-2/3}\,\mathrm{s}^{-5/6}$ for Schoof and $250\,\mathrm{s}^{1/2}\,\mathrm{m}^{-1/2}$ for Budd). Despite this, the Budd friction coefficient is generally smoother than the Schoof friction coefficient, which may be a consequence of the choice of the Tikhonov regularisation
150   coefficient used in the inversion procedure. The Budd friction law also predicts lower mean and median differences between the simulated and observed surface speeds than the Schoof friction law; however, the rmse in the differences are higher than those using the Schoof friction law (Table 2). Finally, in contrast with the Schoof result, there is a negative correlation between N_G and friction coefficient using the Budd friction law, with friction coefficients increasing for decreasing effective pressures ($r^2 = -0.31$; Fig. 5c).

4 Discussion

4.1 The GlaDS effective pressure

The GlaDs-calculated effective pressure in this region of the Antarctic reflects variability in ice thickness and basal topography, with regions of negative effective pressure concentrated in deep basins, subglacial valleys and troughs. The effective pressure in the remainder of the domain, including the interior of the catchment, is close to zero with minimal spatial variation. A region of high effective pressure is found to the north of the Denman trough. In this area, the bed topography is steep and the ice thin; this causes water to drain rapidly and lower the local water pressure. It is unclear whether this is a realistic representation of the basal hydrology in this region or whether the low pressures indicate a limitation of the hydrology model – in situ data collection is necessary to investigate this further.

4.2 Effective pressure and basal sliding laws

Using the Schoof friction law in the ice dynamics inversions, the resulting friction coefficient is smoother when the effective pressure is derived from the GlaDS model run (N_G), compared to when N_O is applied, irrespective of the degree of regularization (Appendix C). When N_O is used, large gradients in the friction coefficient appear that are not aligned with or perpendicular to flow, and naturally increase as the Tikhonov parameter decreases. Previous studies have linked flow-perpendicular gradients in the friction coefficient to topography or hydro-mechanical feedbacks (Sergienko et al., 2014); however, that is unlikely to be the case here given that our gradients are not aligned with or perpendicular to flow. Rather, it is likely that these large gradients in the friction coefficient are artefacts of the inversion procedure that arise only when N_O is used.

Our parameterization for N_O is a function of the ice overburden pressure and bed elevation, $N_O = \rho_i g H + \rho_w g B$, which has been commonly used to define the effective pressure in ice sheet modeling (Budd and Jenssen, 1987; Johnson and Fastook, 2002; Le Brocq et al., 2009). This parameterization is not the actual subglacial hydrology effective pressure, defined as $N = p_i - p_w$, where p_i and p_w are the pressures of ice and water respectively. Indeed, if at the overburden pressure, the effective pressure N should be zero everywhere. However, the definition for N_O used here will produce high effective pressures in regions of thick ice grounded above sea level, and low effective pressure in regions of thick ice grounded below sea level, yielding high friction in interior regions of the Denman catchment (Fig. 3). The water pressure in this parameterization has a dependence on bed elevation, resulting in areas of negative water pressure anywhere the bed is above sea level, which is not physical. Previous studies have investigated alternative parameterizations for the effective pressure in the absence of a coupled ice sheet-subglacial hydrology model. For example, Brondex et al. (2017) use $N = \rho_i g H + \rho_w g B$ for areas grounded below sea level and $N = \rho_i g H$ for areas grounded above sea level, which leads to zero water pressure above sea level. Kazmierczak et al. (2022) used a parameterization that incorporates the effects of till at the base. Our results suggest that ice sheet models would be more accurate with improved representations of the effective pressure in friction laws (e.g. Cook et al., 2022), highlighting the need for further investigation into appropriate parameterizations for the effective pressure when a subglacial hydrology model output is not directly available. To this end, we suggest an alternative parameterization for the effective pressure in section 4.3 below.

Our finding of a positive correlation between N_G and the friction coefficient for the Schoof friction law is unsurprising: effective pressures are lower where there is substantial basal lubrication, which generally leads to a lower friction coefficient

190 and faster surface flow. This is evidence for subglacial hydrology being a key control on the surface speeds in regions of lower effective pressures for the Denman Glacier. However, in the regions of fastest flow at Denman Glacier, particularly towards the grounding line, the model also suggests the presence of substantial channels, which have previously been associated with increasing effective pressures and slowing ice flow (Nienow et al., 2017). The simultaneous presence of channels, fast ice flow, and low effective pressures has also been observed at Aurora Subglacial Basin (Dow et al., 2020) and in the Weddell Sea region

195 (Dow et al., 2022). This is due to the channels being near steady-state which means they operate at effective pressures closer to that of the surrounding distributed system, compared to alpine-like hydrology systems. In the inland regions of the Denman catchment, distributed system effective pressure is also near zero, yet ice flow speed in this region is low. Here, longitudinal friction plays a key role in restraining inland ice flow, with fast flow near the grounding line requiring a combination of high driving stress and low basal effective pressures.

200 The relationship between low effective pressures and low basal friction did not hold for the Budd friction law, despite a stronger negative correlation between the friction coefficient and surface speed for the Budd friction law compared to the Schoof law. Our study uses inverse methods to calculate the friction coefficient for a given τ_b/N_G. For the Budd friction law, this yields a friction coefficient that adjusts to compensate for large variations in basal velocities – the friction coefficient decreases as basal velocities increase and vice versa, and there is a strong inverse relationship between these two fields.

205 However, the requirement for such a strong inverse relationship between friction coefficient and basal velocity leads to a generally weaker relationship between the friction coefficient and the effective pressure, since the effective pressure depends on factors other than the basal velocity: the topography, the ice thickness, and water accumulation along with efficiency of basal channels to some extent. For the Schoof friction law there is no requirement for a strong correlation between the friction coefficient and basal velocities, and we find that spatial variations in the friction coefficient more closely mirror those of the

210 effective pressure, resulting in the stronger correlation between these two fields.

The choice of friction law plays an important role in grounding line migration and mass loss, with studies showing that friction laws that incorporate effective pressure yield more realistic representation of ice sheet dynamics, grounding line retreat, and mass loss than those that do not (Åkesson et al., 2021; Brondex et al., 2019). In an idealized flow line model, Brondex et al. (2017) showed that when using a Weertman friction law, the grounding line can be stable on a retrograde slope, contrary to

215 results from theoretical analysis (Schoof, 2007), and recommended the use of the Schoof law due to its strong physical basis. Coulomb-type friction laws have also demonstrated superior performance over the Budd law in capturing observed grounding line migration (Joughin et al., 2019) and more realistic estimates of future ice mass loss (Brondex et al., 2019). These results are largely a consequence of the cavitation effects captured in Coulomb-type laws, which prevent unphysical, unbounded basal shear stresses for increasing velocities (Schoof, 2005). By contrast, the basal shear stress is unconstrained for finite values of m

220 in other friction laws, including the Weertman or Budd friction laws. Consistent with Brondex et al. (2017, 2019), our results favor the use of a Coulomb-type friction law combined with effective pressure output from the GlaDS model for more realistic representation of the basal friction coefficient calculated using inversion.

The GlaDS model used here has been demonstrated to accurately represent observed properties of the Antarctic subglacial hydrology system (Dow et al., 2018, 2020, 2022). Nevertheless, it has not yet been coupled with an ice sheet model for
225 prognostic simulations of Antarctic ice dynamics. Given the key role that effective pressure plays in friction laws, it is clear that future implementations of ice dynamics models should explicitly take relevant subglacial hydrology processes into account, such as spatially and temporally-variable basal water pressure, if they are to accurately predict climate-driven changes in ice dynamics. A recent study by Kazmierczak et al. (2022) coupled simplified representations of subglacial hydrology to ice dynamics using the Budd friction law. This study by Kazmierczak et al. (2022) examined the impact of different representations
230 of the effective pressure – approximated in turn by height above buoyancy (van der Veen, 1987; Winkelmann et al., 2011), subglacial water depth (Le Brocq et al., 2009), sliding related to water flux (Goeller et al., 2013), and the effective pressure in till (Bueler and Brown, 2009) – on ice mass loss from Antarctica over the 21st Century. A key finding is that when the effective pressure is low in the grounding zone, the ice sheet is more sensitive to increases in climate forcing, ultimately increasing mass loss and resulting in sea level rise. The accuracy of these simplified subglacial hydrology models in representing the
235 full physics of the ice-bed interface still needs to be tested. However, we found that the GlaDS model predicted low effective pressures in the grounding zone of the Denman-Scott catchment, which, following Kazmierczak et al. (2022), suggests this region might be sensitive to enhanced mass loss in the future. The next step is to couple the GlaDS model for a more complex representation of the basal hydrology with an ice dynamics model for application to Antarctic glaciers – an approach that has been applied to Greenland glaciers (e.g. Cook et al., 2022).

240 ## 4.3 Empirical Parameterization

We suggest here an alternative parameterization of effective pressure, N_E, which is empirical in nature and based on spatial patterns in the GlaDS effective pressure output of Denman Glacier. Given the high correlation of water pressure to ice overburden pressure ($r^2 = 0.998$ over the Denman domain) and the relatively constant effective pressure in the interior of Denman, we suggest a form of the water pressure proportional to the ice overburden pressure multiplied by a factor such that the effective
245 pressure reaches a maximum value in areas of high ice thickness. The proposed parameterization is as follows:

$$N_E = \rho_i g H (1 - r_l) \frac{\tilde{H}^m}{\tilde{H}^m + H^m}, \tag{3}$$

$$\tilde{H} = \left(\frac{1-\gamma}{\gamma - r_l}\right)^{1/m} H_t, \tag{4}$$

$$m = \frac{\ln\left(\frac{1-r_l}{\epsilon} - 1\right) + \ln(\gamma - r_l) - \ln(1-\gamma)}{\ln(H_t) - \ln(H_s)}. \tag{5}$$

Here, ρ_i is the density of ice, g is the gravitational acceleration, and H is ice thickness. The effective pressure is given by
250 Eq. 3, with $\tilde{H}$ a constant defined by Eq. 4 and m a constant exponent defined by Eq. 5. γ is a constant representing typical effective pressure as a fraction of overburden in areas high ice thickness; r_l is the water pressure as a fraction of overburden as the ice thickness goes to zero; H_t is a typical large ice thickness; H_s is a typical small ice thickness; and ϵ is a small constant taken so that in areas of low ice thickness (H_s) the water pressure is at a typically low value $(r_l + \epsilon)\rho_i g H$. GlaDS output

effective pressure and ice thickness data for the Denman Glacier was used to find values for r_l, δ, H_s, and H_t used in N_E

255 (ϵ was taken to equal 0.05). This resulted in $r_l = 0.7$, $\delta = 0.96$, $H_s = 500\,\mathrm{m}$, and $H_t = 2800\,\mathrm{m}$. The empirical nature of this parameterization means that these constants are not "optimized" and use of N_E on future glaciers may require an alteration of these constants, specifically H_s and H_t which can be determined using ice thickness data. More details on the parameterization and its derivation are provided in Appendix E.

The proposed empirical effective pressure (N_E), is compared with the GlaDS output effective pressure (N_G), N_O, and

260 the Brondex et al. (2017) prescribed effective pressure – all as a fraction of overburden pressure (Fig. 6). N_E matches the GlaDS output effective pressure more closely than both N_O and the Brondex et al. (2017) prescribed effective pressures (note the different color bar scalings in Fig. 6a,b compared with Fig. 6c,d). This is further illustrated in Fig. 6f, which shows the difference between N_E and N_G as a fraction of overburden pressure: 72.9 % of the domain has a difference of <0.02, and 95.6 % of the domain has a difference of <0.05. Fig. 6e shows the saturation term as well as the physically equivalent scatter

265 from the GlaDS output data. The form of the scatter is qualitatively similar to the saturation term in areas of moderate to high ice thickness. The mean percent difference excluding the area of the domain where $N_G \leq 0$, given by $|N_E/N_G - 1|$, is 118 %, though 45.4 % of this domain falls below 20 % and 77.0 % of the domain falls below 50 % so the data is skewed from the areas of low effective pressure. Standing alone, this does not sound impressive and it is a result of the variability of the scatter seen in Fig. 6e. This is still a substantial improvement over N_O which has a mean percent difference of 3688 % where 57.7 % of the

270 domain falls between 2000 % and 3000 % difference.

Though this parameterization is not derived from physical principles and it lacks complete hydrological connectivity to the ocean, it produces physically realizable effective pressures $0 < N < \rho_i g H (1 - r_l)$, which match closely to GlaDS output effective pressures over Denman Glacier. The success of our empirical parameterization over N_O on Denman Glacier combined with its improved physical implications over N_O warrants further investigation into its validity and potential use in future

275 modeling studies, particularly on Antarctic glaciers.

5 Conclusions

The Denman-Scott catchment in East Antarctica is a region that is undergoing active glacial retreat and is vulnerable to ongoing mass loss as the climate warms. We have investigated the coupled interactions between the subglacial hydrological system and the ice sheet through the basal friction coefficient – an important tuning parameter used in friction laws – and its dependence

280 on the form of the effective pressure. We find that when the Schoof friction law is used, a smoother friction coefficient and slightly improved match between the simulated and observed velocities is found when an effective pressure derived directly from GlaDs is used, compared to when an effective pressure equal to the ice overburden pressure plus the gravitational potential energy of water (N_O) is used. Of the two friction laws tested here – the Schoof friction law and the Budd friction law – only the Schoof friction law captures the predicted relationship between the subglacial hydrological and the ice sheet dynamics. That

285 is, using the Schoof law, regions of lower effective pressures tend to also have lower simulated basal friction and faster flow – evidence for the controlling role of the hydrological system.
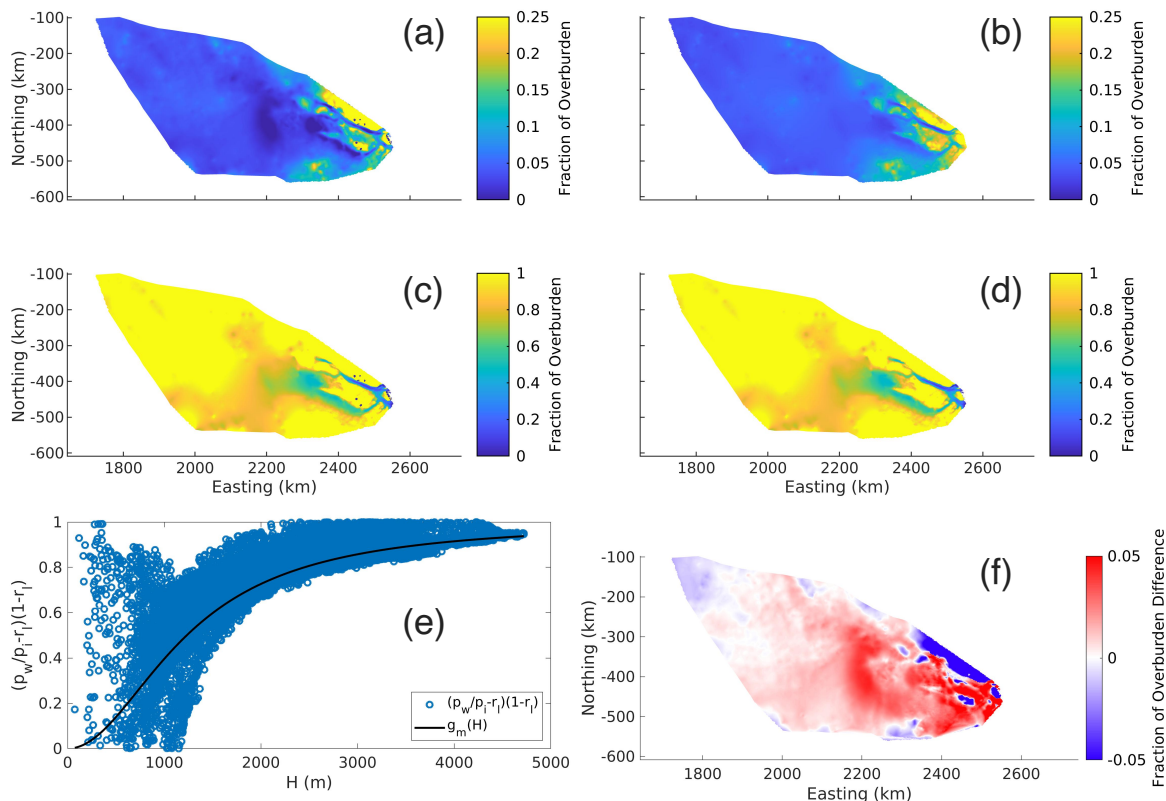
Figure 6. Effective pressures from: **(a)** the GlaDS simulation, **(b)** the proposed empirical parameterization in Eq. 3, **(c)** typically prescribed (N_O), and **(d)** Brondex et al. (2017). **(e)** The saturation curve and the physically equivalent scatter for GlaDS effective pressure. **(f)** The difference between the proposed empirical parameterization (N_E) and the GlaDS effective pressures as a fraction of overburden.

In their application of the GlaDs model to the Aurora Subglacial Basin, Dow et al. (2020) showed the utility of geophysical observations in validating and constraining subglacial hydrology model parameterizations. By contrast with the Aurora Subglacial Basin, the Denman-Scott catchment is a relatively sparsely observed system, with few observations available to constrain our model simulations. Similarly to previous studies (Dow et al., 2020; Schroeder et al., 2013; Hager et al., 2022), we recommend the collection of: high-resolution radar surveys, with a particular focus on the regions at the boundary of the distributed and channelized subglacial hydrology systems and over the lake-like features upstream of the Denman and Scott channels; and direct measurement of subglacial hydrological flux across the grounding line to constrain simulated subglacial meltwater volumes. Such observations are vital in understanding the role of the subglacial hydrological system and its coupled feedbacks with the ice sheet.

We proposed a new parameterization for the effective pressure based on empirical data of the Denman-Scott catchment and the GlaDS results, that more closely matches simulated effective pressures than suggestions from previous literature, and

which shows promise in capturing key features of the subglacial system in the absence of a complete subglacial hydrology model output. However, given the empirical nature of this parameterization, our results highlight the importance of simulating
300 coupled interactions between the subglacial hydrology and ice sheet systems to accurately represent ice sheet flow, and future work should focus on coupling of these two systems in transient simulations of the Antarctic Ice Sheet.

Appendix A: Grid domains and effective pressure extrapolation

The domains of the ISSM and GlaDS models differ, with the GlaDS domain being a subset of the ISSM domain. This means that there are regions within the ISSM domain for which GlaDS effective pressures do not exist. Here, we test the impact of
305 two different methods to extrapolate the effective pressure in regions outside the GlaDS domains. The first method relates the GlaDS effective pressure to the bed topography and surface speeds. We first partition the domain into three regions based on surface speed, with the first encompassing areas where $v<500\,\mathrm{m\,a^{-1}}$, the second where $500\geq v<1000\,\mathrm{m\,a^{-1}}$, and the third where $v\geq1000\,\mathrm{m\,a^{-1}}$. We then calculate a linear regression between the bed topography and the GlaDS effective pressures in each region, and linearly extrapolate the effective pressure onto the ISSM domain based on this relationship. The regression
310 coefficients are shown in Table A1. The second method uses the ice overburden pressure plus the gravitational potential energy of the water. The resulting effective pressure is shown in Fig. A1. The friction coefficient found using method two is generally more smooth than the friction coefficient found using method one, with the exception of transition areas between the GlaDS and extrapolated effective pressures far to the west and south of the GlaDS domain. The match between the simulated and observed surface speeds are similar for the two extrapolations, though method two produces more variation in the region upstream of the
315 grounding line than method one.

Regression coefficient	$v<500\,\mathrm{m\,a^{-1}}$	$500\geq v<1000\,\mathrm{m\,a^{-1}}$	$v\geq1000\,\mathrm{m\,a^{-1}}$
α	286	-248	136
β	1.28×10^6	8.03×10^5	1.11×10^6

Table A1. Linear regression coefficients α and β for the relationship $N = \alpha B + \beta$, where N is the GlaDS effective pressure and B is the bed elevation.

In general, there is no reason that the hydrology and ice dynamics basins should match exactly, and where this is the case, we would always expect regions where we will need to extrapolate boundary conditions between the models. The fact that we have had to extrapolate effective pressure is not in itself a problem, and our results show the importance of taking into consideration the method of extrapolation. Importantly, there may be other methods for extrapolating the boundary conditions that we did not
320 consider, including parameterising the effective pressure using different physical assumptions (e.g. Bueler and Brown, 2009; Goeller et al., 2013; Le Brocq et al., 2009; van der Veen, 1987; Winkelmann et al., 2011), and future studies should establish best practice in this regard.
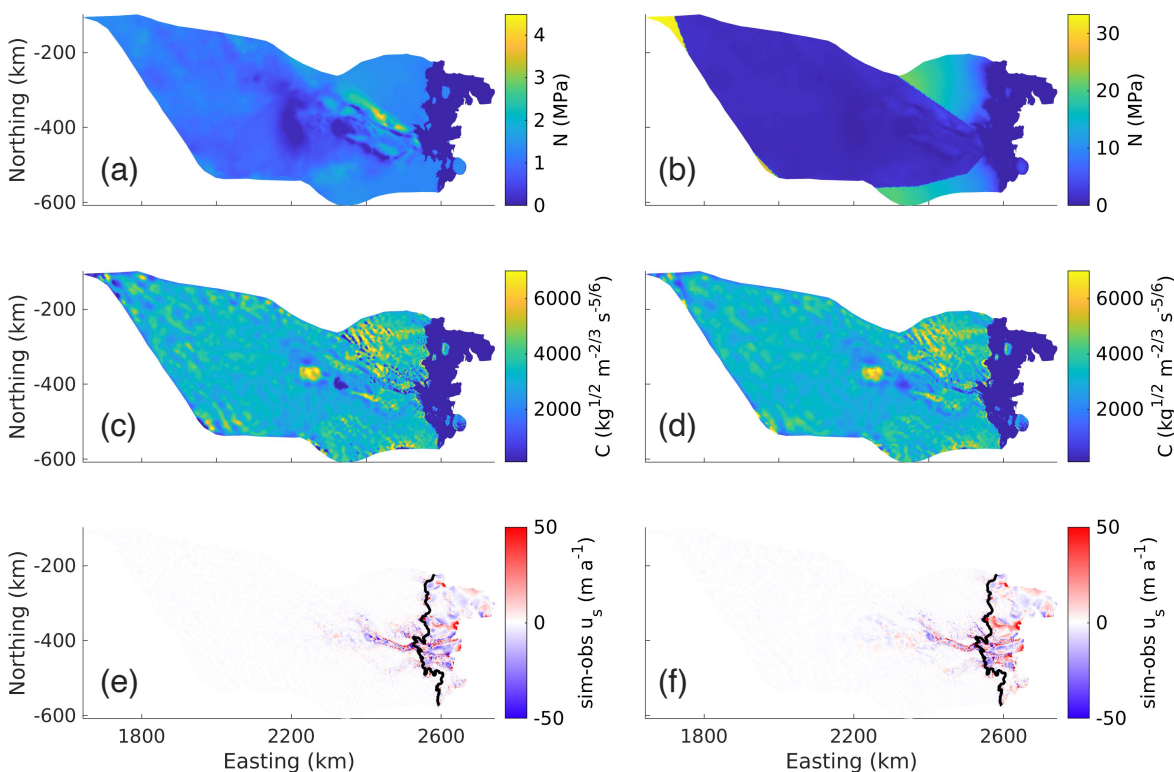
Figure A1. **(a)**-**(b)** Effective pressures (MPa); **(c)**-**(d)** friction coefficients estimated using inversion of the Schoof friction law ($\mathrm{kg}^{1/2}\,\mathrm{m}^{-2/3}\,\mathrm{s}^{-5/6}$); and **(e)**-**(f)** mismatch between the simulated and observed surface speeds ($\mathrm{m\,a}^{-1}$). The left column **(a)**, **(c)**, **(e)** shows results for extrapolation method 1 and the right column **(b)**, **(d)**, **(f)** shows results for method 2. In each panel, the black lines are the grounding lines, and the $x-$ and $y-$coordinates are polar stereographic, referenced to WGS84.

Appendix B: Mesh sensitivity

Depending on the degree of regularisation in the inverse method, small-scale features may be present in the friction coefficient.
325 Here, we perform a sensitivity analysis to examine the extent to which such features arise due to the details of the mesh: the exact placement of the nodes and vertices. We generate five different meshes by adding a random perturbation in the surface velocity field of up to 20 % of the original MEaSUREs velocities (Rignot et al., 2011; Rignot, 2017), and then perform anisotropic mesh refinement on the velocity magnitude, as follows: the typical edge length of the elements is 3000 m; for regions where the surface speed is $\geq$500 m a^{-1}, maximum edge lengths are 500 m; and for regions where the surface speed is
330 between 100 and 500 m a^{-1}, the maximum edge length is 2000 m. Elements close to the grounding line have a maximum edge length of 1000 m.

Using each of these five meshes, we calculate the Budd and Schoof friction coefficients. The probability distributions of the normalized friction coefficients are shown in Fig. B1. The mean and standard deviation of the differences between both the Schoof and the Budd friction coefficients for the perturbed mesh simulations and that of the original mesh are smaller

335 in magnitude than the mean and standard deviation of the difference between the friction coefficients using GlaDS and the prescribed effective pressure B1. Hence, the choice of the mesh used has less of an impact on the friction coefficients than the effective pressure used.

Comparison Model	Mean of Difference	Standard Deviation of Difference
Prescribed (Budd)	370	207
Noise 1 (Budd)	-0.640	15.4
Noise 2 (Budd)	-1.18	22.2
Noise 3 (Budd)	-0.531	20.6
Noise 4 (Budd)	11.9	84.8
Noise 5 (Budd)	-2.22	18.7
Prescribed (Schoof)	55.0	512
Noise 1 (Schoof)	-23.5	369
Noise 2 (Schoof)	-22.9	312
Noise 3 (Schoof)	-21.1	411
Noise 4 (Schoof)	-5.67	353
Noise 5 (Schoof)	-25.7	315

Table B1. Mean and standard deviation of the difference between friction coefficients for various model inputs. The GlaDS input effective pressure with the mesh used in the manuscript simulations is the model being compared to. "Noise x" refers to different perturbed meshes with N_G input effective pressure and "Prescribed" refers to using N_O instead of N_G but with the mesh used in the manuscript simulations. The Schoof friction coefficient has units of $\mathrm{kg}^{1/2}\,\mathrm{m}^{-2/3}\,\mathrm{s}^{-5/6}$ and the Budd friction coefficient has units of $\mathrm{s}^{1/2}\,\mathrm{m}^{-1/2}$.
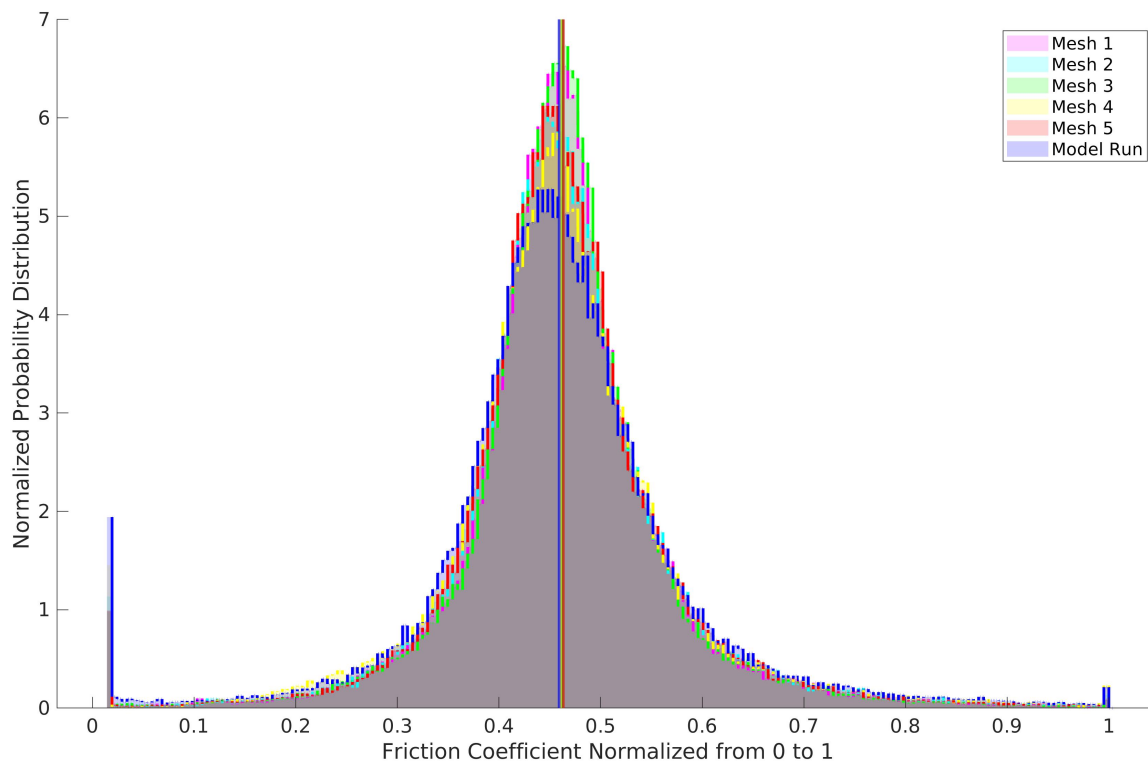
Figure B1. Normalized probability distribution functions for the Schoof friction coefficient for the computational mesh and five perturbed meshes. Vertical lines indicate the mean of each distribution.

Appendix C: Inversion procedure

The Budd friction law is given by

$$\tau_b = \alpha^2 N u_b, \tag{C1}$$

340

where τ_b is the basal shear stress (Pa), α is the friction coefficient ($\mathrm{s}^{1/2}\,\mathrm{m}^{-1/2}$), N is the effective pressure (Pa), and u_b is the basal sliding velocity ($\mathrm{m\,a}^{-1}$), which for SSA is equal to the surface velocity. Here, N is taken as direct output from the GlaDS model (N_G), or specified by $N_O = \rho_i g H + \rho_w g B$ where g is the gravitational acceleration ($\mathrm{m\,s}^{-2}$), H is the ice thickness (m), B is the bed elevation (m), ρ_i is the ice density ($\mathrm{kg\,m}^{-3}$), and ρ_w is the water density ($\mathrm{kg\,m}^{-3}$). When using N_G, we apply a lower cap of 1% of ice overburden pressure (see section D below).

345

We use inverse methods to calculate the basal friction coefficient α from the Budd friction law and the ice rigidity in the Glen flow law. The inverse method works to reduce the mismatch between the simulated and observed velocities, here taken from MEaSUREs v2 (Rignot et al., 2011; Rignot, 2017), by minimising a cost function that includes both linear and logarithmic
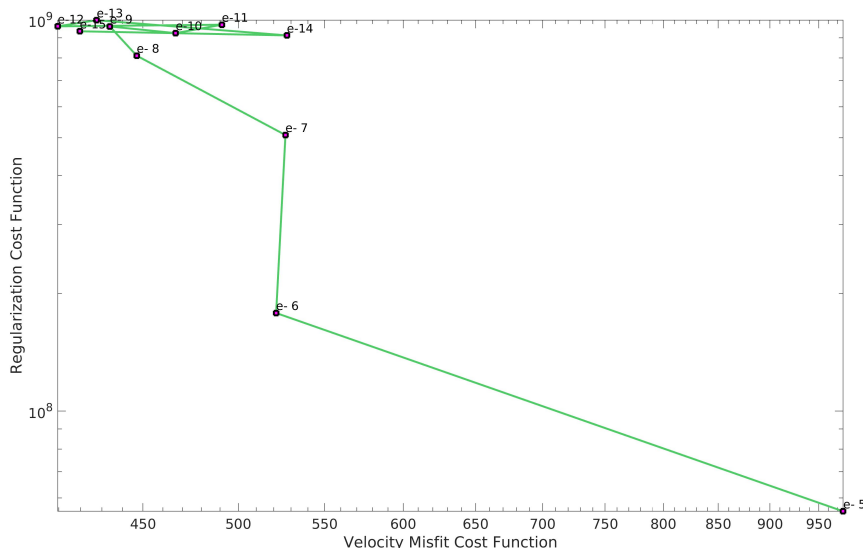
Figure C1. L-curve analysis for the Budd friction coefficient with GlaDS input effective pressure (4.5% cap and ice overburden pressure outside the GlaDS domain)

velocity misfit components. We also include a Tikhonov regularisation term that penalizes strong gradients in the friction
350   coefficient, and hence prevents overfitting.

We perform the following inversion procedure. First, we invert for the ice rigidity over the floating portion of the domain. Next, we invert for the Budd friction coefficient over the grounded portion of the domain, using an ice rigidity on grounded ice specified by the Paterson function and temperatures from RACMOv2.3 (van Wessem et al., 2018). Finally, an inversion for the ice rigidity over the entire domain was performed. The linear and logarithmic cost function coefficients were chosen so
355   that their contributions to the total cost function would differ by an order one factor. An L-curve analysis (Fig. C1; Hansen, 2000) was used during the second inversion to determine a suitable Tikhonov regularisation coefficient. For the ice rigidity inversions, the Tikhonov regularisation parameter was chosen so that its contribution to the total cost function differed by an order one factor from that of the linear misfit. The final friction coefficients are shown in Fig. C3, their distribution in Fig. C4, and the final rigidities in Fig. C5.
360   The Schoof friction law is given by the following:

$$\tau_b = \frac{C^2 |u_b|^{m-1}}{1 + (C^2/(C_{\max}N))^{1/m} |u_b|} u_b, \tag{C2}$$

where C is the Schoof friction coefficient, and $C_{\max}$ is Iken's bound, here $C_{\max} = 0.8 \, \mathrm{m}^{-1/3} \, \mathrm{s}^{1/3}$. We used the friction coefficient estimated using the Budd friction law to compute an initial estimate of the friction coefficient for the Schoof friction law. We then perform an inversion for the friction coefficient as per the method described above for the Budd friction law (capping
365   N_G at 0.4 % of overburden this time).
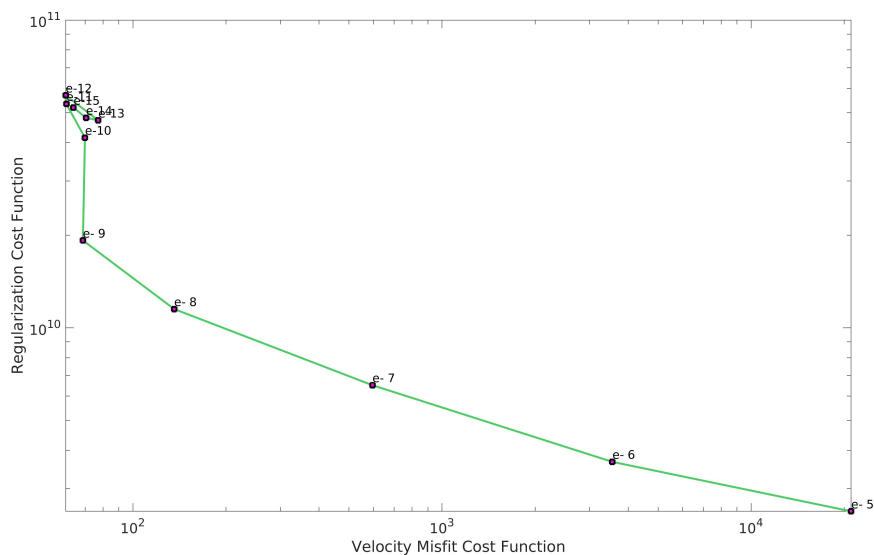
Figure C2. L-curve analysis for the Schoof friction coefficient with GlaDS input effective pressure (4.5% cap and ice overburden pressure outside the GlaDS domain)
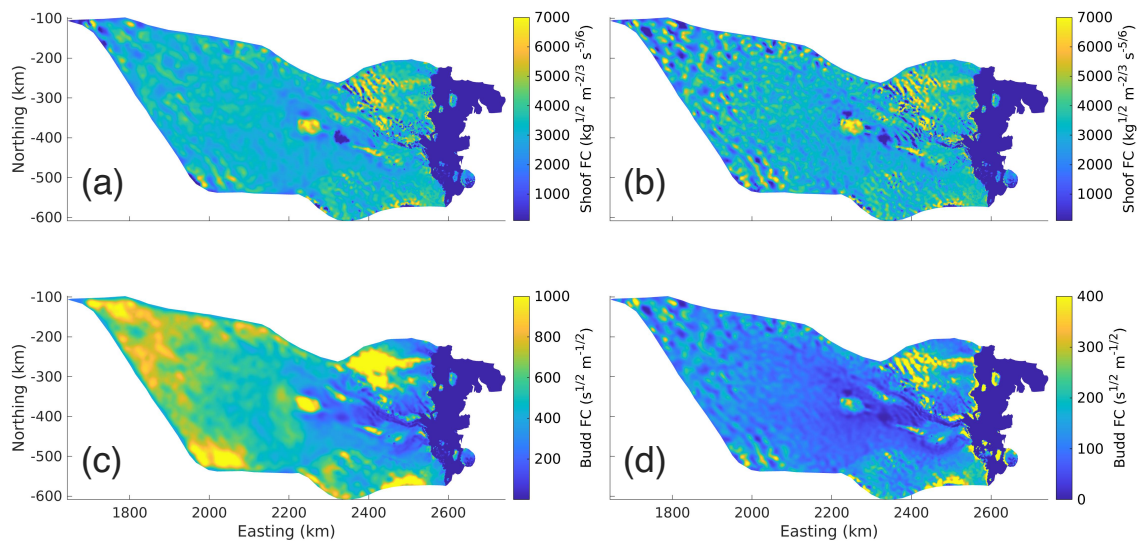
Figure C3. Friction coefficients from inversion. **(a)** Schoof friction coefficient from N_G run; **(b)** Schoof friction coefficient from N_O run; **(c)** Budd friction coefficient from N_G run; and **(d)** Budd friction coefficient from N_O run.
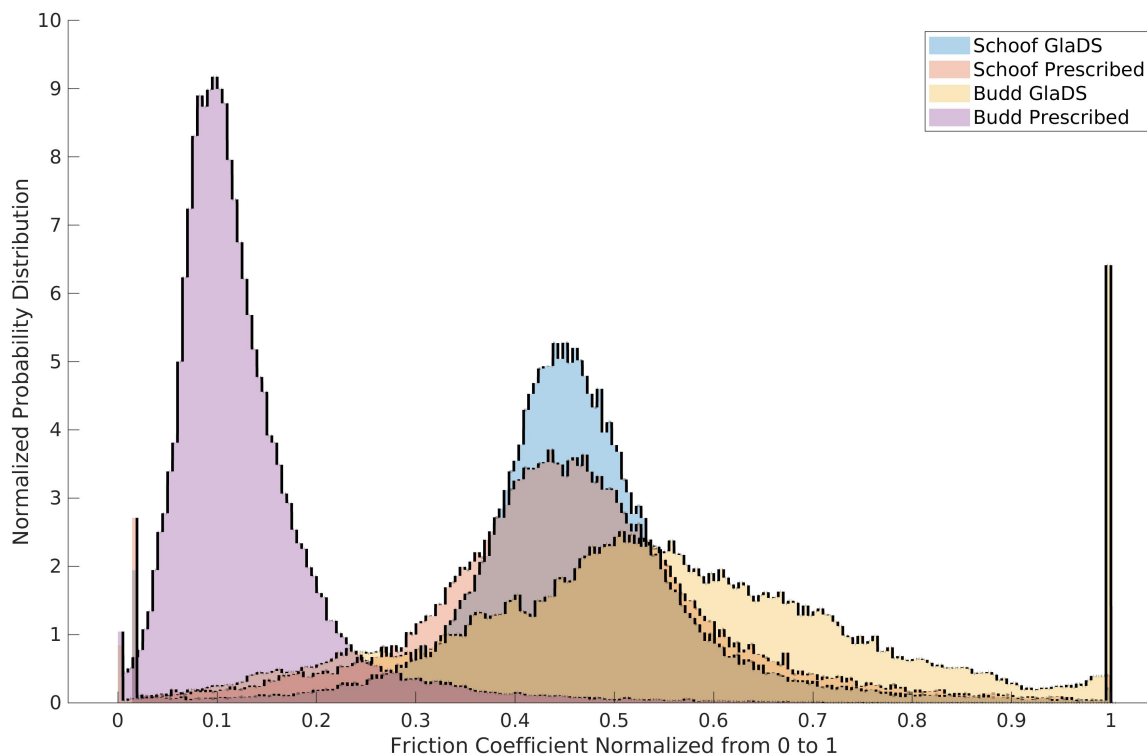
Figure C4. Probability distributions of the normalized friction coefficients for the Budd and Schoof friction laws with GlaDS and prescribed effective pressures.

The cost function coefficients for the various model runs are displayed in Table C1.

Cost Function Coefficient	Value I1	Value I2	Value I3	Value I4	Value I5
Linear	8000	2000	8000	200	8000
Logarithmic	60	10	25	2	25
Tikhonov	10^{-18}	10^{-6}	10^{-18}	10^{-9}	10^{-18}

Table C1. Cost function coefficients for each inversion. I1 ice rigidity over ice shelf; I2 Budd friction coefficient over grounded domain; I3 ice rigidity over entire domain; I4 Schoof friction coefficient over the grounded domain; and I5 ice rigidity over the entire domain.
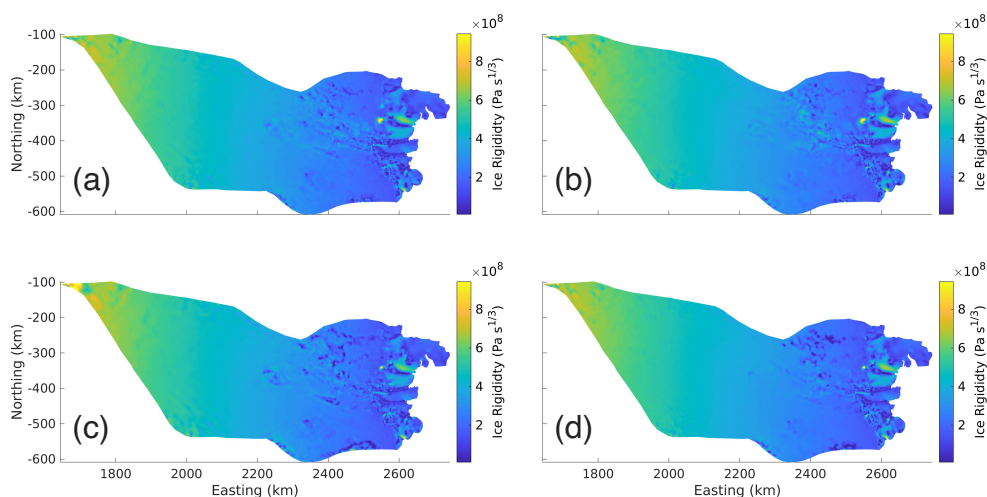
Figure C5. Ice Rigidities from inversion. **(a)** Ice rigidity from Schoof N_G run; **(b)** Ice rigidity from Schoof N_O run; **(c)** Ice rigidity from Budd N_G run; and **(d)** Ice rigidity from Budd N_O run

Appendix D: Effective pressure cap

For regions of very low or negative effective pressure, the basal shear stresses are also very low or almost vanish. In these regions, the inverse method compensates by increasing the friction coefficient upstream of the anomalously low effective
370   pressure, leading to an underestimate of surface speeds there compared with the observations. The surface speeds are also generally overestimated in the region of vanishing shear stresses.

To account for this, we adjust the effective pressure in regions of low or negative effective pressure, capping the minimum as a percentage of the overburden pressure. Fig. D1 shows the effective pressures from GlaDS model output interpolated onto the ISSM mesh, and for caps of 0.2 %, 0.4 %, 2 % and 4 %. We find that a cap of 0.4 % of overburden is required to avoid
375   this artefacting. For a cap of 0.4 %, approximately 2 % of the domain has an effective pressure that is linearly proportional to the overburden (Fig. D2). That is, 98 % of the effective pressure in the ISSM simulation is derived directly from the GlaDS simulated effective pressure.
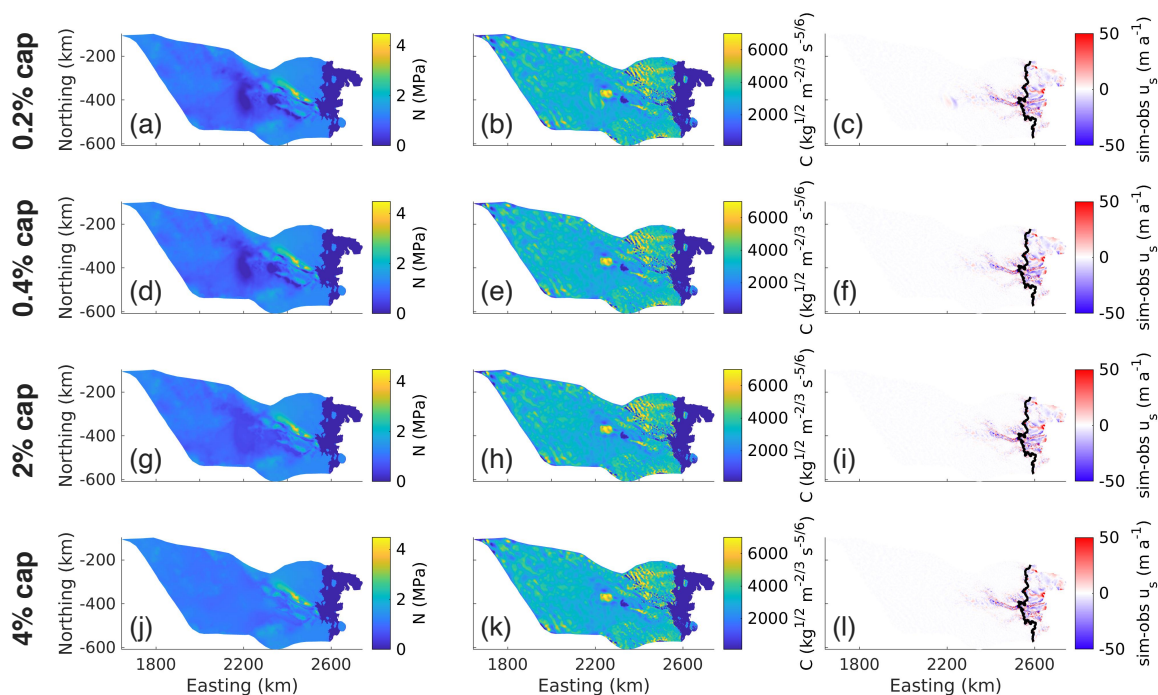
Figure D1. Effective pressure cap analysis. Effective pressures are shown in **(a)**, **(d)**, **(g)**, **(j)**; friction coefficients **(b)**, **(e)**, **(h)**, **(k)**; mismatch between simulated and observed surface speeds **(c)**, **(f)**, **(i)**, **(l)**. Upper row 0.2 % cap; second row 0.4 % cap; third row 2 % cap; last row 4 % cap.
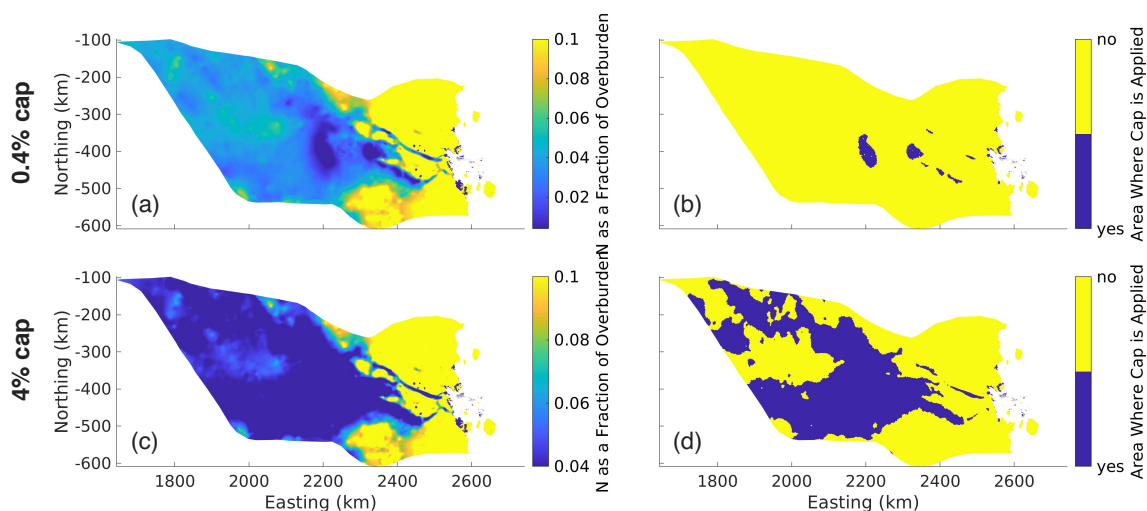
Figure D2. Effective pressure caps. **(a)** and **(c)** show the effective pressure. **(b)** and **(d)** show the area where the cap is applied (dark blue).

Appendix E: Empirical effective pressure parameterization

We propose a new effective pressure parameterization that is empirical in nature and based on the GlaDS effective pressure
output in the Denman-Scott catchment. Effective pressure is defined as $N = p_i - p_w$ where $p_i = \rho_i g H$ is the ice overburden
pressure and p_w is the water pressure. In this equation, p_i is well known; however, p_w is generally poorly known in Antarctica
due to few direct measurements. Hence, a more robust parameterization of the effective pressure requires a physically-realistic
prescription for this water pressure. The proposed parameterization uses the fact that water pressure has a high correlation
with overburden pressure ($r^2 = 0.998$ over the Denman domain) and that water pressure as a fraction of overburden pres-
sure maintains some value for small ice thicknesses and saturates near 1 for large ice thickness. We suggest the following
parameterization for water pressure:

$$p_w = \rho_i g H \left(r_l + (1 - r_l) g_m(H) \right), \tag{E1}$$

where r_l is the maximum allowable ratio of effective pressure to ice overburden pressure and $g_m(H)$ is a saturation term. We
specify $g_m(H)$ as follows:

$$g_m(H) = \frac{H^m}{\tilde{H}^m + H^m}. \tag{E2}$$

Here, $\tilde{H}$ is a constant thickness, which is chosen so that an area where water is expected to be pressurized with fraction of
overburden γ will reach this level of pressurization by ice thickness H_t. This yields an $\tilde{H}$ of the following form:

$$\tilde{H} = \left(\frac{1 - \gamma}{\gamma - r_l} \right)^{1/m} H_t \tag{E3}$$

The only parameter left to be determined is m, and here we choose a value of m so that at a typically small ice thickness, H_s,
the water pressure as a fraction of overburden pressure will be slightly above the minimum allowed water pressure $p_w(H) =$
$(r_l + \epsilon) \rho_i g H$ where ϵ is a constant introduced with the purpose of having the saturation term concave down even in areas where
there is low ice thickness on the glacier.

We rearrange Eq. (E3) to solve for m as follows:

$$m = \frac{\ln \left(\frac{1 - r_l}{\epsilon} - 1 \right) + \ln(\gamma - r_l) - \ln(1 - \gamma)}{\ln(H_t) - \ln(H_s)}. \tag{E4}$$

Using Eq. (E1), we derive the following expression for the effective pressure, with $\tilde{H}$ from Eq. (E3) and m from Eq. (E4):

$$N = \rho_i g H (1 - r_l) \frac{\tilde{H}^m}{\tilde{H}^m + H^m}. \tag{E5}$$

The empirical nature of this parameterization brings into question its physical validity. Unlike N_O and the Brondex et al.
(2017) prescribed effective pressure, the effective pressure proposed in Eq. (E5) does not have complete hydrological con-
nectivity to the ocean at the grounding line. However, N_O and the Brondex et al. (2017) prescribed effective pressure can
obtain values of negative or zero water pressure, which is nonphysical. The effective pressure proposed in Eq. (E5) can reach
a minimum water pressure of $p_w = r_l \rho_i g H$ meaning that it will always give a physically possible value of effective pressure.

Delving further into the implications of these effective pressure parameterizations, we see that the hydraulic potential is given by $\phi = N_O - N$ (Werder et al., 2013), which means that using N_O gives a constant hydraulic potential and a stagnant subglacial hydrology system. The Brondex et al. (2017) prescribed effective pressure implies constant hydraulic potential for bed elevations below sea level and $\phi = \rho_w g B$, where B is the bed elevation, for bed elevations above sea level. Which means that water does not flow when the bed elevation is below sea level, and it flows entirely due to gravity when the bed elevation is above sea level. Taking the gradient in the hydraulic potential for the proposed effective pressure parameterization yields the following equation:

$$\overrightarrow{\nabla}\phi = \rho_i g f_B(H)\overrightarrow{\nabla}H + \rho_w g\overrightarrow{\nabla}B, \tag{E6}$$

$$f_B(H) = r_l \frac{1 + (1-m)(H/\tilde{H})^m}{(1+(H/\tilde{H})^m)^2}. \tag{E7}$$

Here, $f_B(H)$ is a dimensionless factor which describes the extent to which ice thickness gradients play a role in the hydraulic potential gradient. It is seen that in the regime of larger ice thickness $f_B(H)$ goes to 0, and the gradient in the bed elevation becomes the sole control on the direction of water flow; in the regime of small ice thickness $f_B(H)$ goes to r_l, and gradients in the ice thickness become of similar importance to gradients in the bed elevation. This is a more intuitive picture of the subglacial hydrological system, where water can flow throughout the entire domain, and where flow is dependent on both the basal topography and the ice thickness, as is expected.

Except for the lack of complete hydrological connectivity to the ocean, the proposed parameterization in Eq. (E5) agrees more closely with our understanding of subglacial hydrology than both N_O and the Brondex et al. (2017) prescribed effective pressures. The improved performance over N_O and the Brondex et al. (2017) prescribed effective pressures for the Denman Glacier is encouraging, and warrants further exploration, including exploring the validity of this parameterization compared with subglacial hydrology model outputs and its potential use in future modeling studies where full ice sheet-subglacial hydrology model coupling is unfeasible. Improvements to this parameterization, such as adding in the effects of ice velocity, may improve upon the performance of this parameterization.

Code and data availability. We use version 4.21 of the open-source ISSM software, which is freely available for download from https://issm.jpl.nasa.gov/download/. The datasets used to initialize GlaDS and ISSM are publicly available and cited in the main body of the text. GlaDS hydrology outputs and ISSM friction coefficients for the Denman-Scott catchment are available at Zenodo repository 7709384

Author contributions. KRM designed and completed the ISSM model runs and produced figures; CD ran the GlaDS model; FSM and CD provided project direction. All authors wrote the manuscript.

Competing interests. The authors declare no competing interests are present.

435   *Acknowledgements.* FSM was supported under an Australian Research Council (ARC) Discovery Early Career Research Award (DE210101433) and the ARC Special Research Initiative Securing Antarctica's Environmental Future (SR200100005). CFD was supported by the Natural Sciences and Engineering Research Council of Canada (RGPIN-03761-2017) and the Canada Research Chairs Program (950-231237). We thank the Digital Research Alliance of Canada for access to supercomputer resources.

References

440 Adusumilli, S., Fricker, H. A., Medley, B., Padman, L., and Siegfried, M. R.: Interannual Variations in Meltwater Input to the Southern Ocean from Antarctic Ice Shelves, Nature Geoscience, 13, 616–620, https://doi.org/10.1038/s41561-020-0616-z, 2020.

Åkesson, H., Morlighem, M., O'Regan, M., and Jakobsson, M.: Future Projections of Petermann Glacier Under Ocean Warming Depend Strongly on Friction Law, Journal of Geophysical Research: Earth Surface, 126, e2020JF005 921, https://doi.org/10.1029/2020JF005921, 2021.

445 Beaud, F., Aati, S., Delaney, I., Adhikari, S., and Avouac, J.-P.: Surge dynamics of Shisper Glacier revealed by time-series correlation of optical satellite images and their utility to substantiate a generalized sliding law, The cryosphere, 16, 3123–3148, 2022.

Brancato, V., Rignot, E., Milillo, P., Morlighem, M., Mouginot, J., An, L., Scheuchl, B., Jeong, S., Rizzoli, P., Bueso Bello, J. L., and Prats-Iraola, P.: Grounding Line Retreat of Denman Glacier, East Antarctica, Measured With COSMO-SkyMed Radar Interferometry Data, Geophysical Research Letters, 47, e2019GL086 291, https://doi.org/10.1029/2019GL086291, 2020.

450 Brondex, J., Gagliardini, O., Gillet-Chaulet, F., and Durand, G.: Sensitivity of Grounding Line Dynamics to the Choice of the Friction Law, J. Glaciol., 63, 854–866, https://doi.org/10.1017/jog.2017.51, 2017.

Brondex, J., Gillet-Chaulet, F., and Gagliardini, O.: Sensitivity of Centennial Mass Loss Projections of the Amundsen Basin to the Friction Law, The Cryosphere, 13, 177–195, 2019.

Budd, W. F. and Jenssen, D.: Numerical Modelling of the Large-Scale Basal Water Flux under the West Antarctic Ice Sheet, in: Dynamics of

455 the West Antarctic Ice Sheet, edited by Van der Veen, C. J. and Oerlemans, J., Glaciology and Quaternary Geology, pp. 293–320, Springer Netherlands, Dordrecht, https://doi.org/10.1007/978-94-009-3745-1_16, 1987.

Budd, W. F., Keage, P., and Blundy, N.: Empirical Studies of Ice Sliding, Journal of Glaciology, 23, 157–170, 1979.

Bueler, E. and Brown, J.: Shallow Shelf Approximation as a "Sliding Law" in a Thermomechanically Coupled Ice Sheet Model, Journal of Geophysical Research, 114, 1–21, https://doi.org/10.1029/2008JF001179, 2009.

460 Cook, S. J., Christoffersen, P., and Todd, J.: A Fully-Coupled 3D Model of a Large Greenlandic Outlet Glacier with Evolving Subglacial Hydrology, Frontal Plume Melting and Calving, Journal of Glaciology, 68, 486–502, https://doi.org/10.1017/jog.2021.109, 2022.

Dow, C., Werder, M., Babonis, G., Nowicki, S., Walker, R., Csatho, B., Morlighem, M., Dow, C. F., Werder, M. A., Babonis, G., Nowicki, S., Walker, R. T., Csatho, B., and Morlighem, M.: Dynamics of Active Subglacial Lakes in Recovery Ice Stream, Journal of Geophysical Research, 123, 837–850, https://doi.org/10.1002/2017JF004409, 2018.

465 Dow, C., McCormack, F., Young, D., Greenbaum, J., Roberts, J., and Blankenship, D.: Totten Glacier Subglacial Hydrology Determined from Geophysics and Modeling, Earth and Planetary Science Letters, 531, 115 961, https://doi.org/10.1016/j.epsl.2019.115961, 2020.

Dow, C. F., Ross, N., Jeofry, H., Siu, K., and Siegert, M. J.: Antarctic Basal Environment Shaped by High-Pressure Flow through a Subglacial River System, Nature Geoscience, 15, 892–898, https://doi.org/10.1038/s41561-022-01059-1, 2022.

Gagliardini, O., Cohen, D., Raback, P., and Zwinger, T.: Finite-Element Modeling of Subglacial Cavities and Related Friction Law, Journal

470 of Geophysical Research - Earth Surface, 112, 1–11, https://doi.org/10.1029/2006JF000576, 2007.

Goeller, S., Thoma, M., Grosfeld, K., and Miller, H.: A Balanced Water Layer Concept for Subglacial Hydrology in Large-Scale Ice Sheet Models, The Cryosphere, 7, 1095–1106, https://doi.org/10.5194/tc-7-1095-2013, 2013.

Greene, C. A.: RAMP Radarsat Antarctic Mapping Project, https://www.mathworks.com/matlabcentral/fileexchange/52031-ramp-radarsat-antarctic-mapping-project, 2022.

475   Greene, C. A., Gwyther, D. E., and Blankenship, D. D.: Antarctic Mapping Tools for Matlab, Computers & Geosciences, 104, 151–157, https://doi.org/10.1016/j.cageo.2016.08.003, 2017.

Hager, A. O., Hoffman, M. J., Price, S. F., and Schroeder, D. M.: Persistent, Extensive Channelized Drainage Modeled beneath Thwaites Glacier, West Antarctica, The Cryosphere, 16, 3575–3599, https://doi.org/10.5194/tc-16-3575-2022, 2022.

Hansen, P. C.: The L-Curve and Its Use in the Numerical Treatment of Inverse Problems, in: In Computational Inverse Problems in Electro-
480   cardiology, Ed. P. Johnston, Advances in Computational Bioengineering, pp. 119–142, WIT Press, Southampton, 2000.

Iken, A. and Bindschadler, R. A.: Combined Measurments of Subglacial Water-Pressure and Surface Velocity of Findelengletsher, Switzer-land, Journal of Glaciology, 32, 101–119, 1986.

Indrigo, C., Dow, C. F., Greenbaum, J. S., and Morlighem, M.: Drygalski Ice Tongue Stability Influenced by Rift Formation and Ice Mor-phology, Journal of Glaciology, 67, 243–252, https://doi.org/10.1017/jog.2020.99, 2021.

485   Johnson, J. and Fastook, J. L.: Northern Hemisphere Glaciation and Its Sensitivity to Basal Melt Water, Quaternary International, 95–96, 65–74, https://doi.org/10.1016/S1040-6182(02)00028-9, 2002.

Joughin, I., Smith, B. E., and Schoof, C. G.: Regularized Coulomb Friction Laws for Ice Sheet Sliding: Application to Pine Island Glacier, Antarctica, Geophysical Research Letters, 46, 4764–4771, 2019.

Kazmierczak, E., Sun, S., Coulon, V., and Pattyn, F.: Subglacial Hydrology Modulates Basal Sliding Response of the Antarctic Ice Sheet to
490   Climate Forcing, Preprint, Ice sheets/Numerical Modelling, https://doi.org/10.5194/tc-2022-53, 2022.

Larour, E., Seroussi, H., Morlighem, M., and Rignot, E.: Continental Scale, High Order, High Spatial Resolution, Ice Sheet Modeling Using the Ice Sheet System Model (ISSM), Journal of Geophysical Research, 117, 1–20, https://doi.org/10.1029/2011JF002140, 2012.

Le Brocq, A., Payne, A., Siegert, M., and Alley, R.: A Subglacial Water-Flow Model for West Antarctica, Journal of Glaciology, 55(193), 879–888, 2009.

495   MacAyeal, D.: Large-Scale Ice Flow over a Viscous Basal Sediment: Theory and Application to Ice Stream B, Antarctica, Journal of Geo-physical Research, 94, 4071–4087, 1989.

Morlighem, M., Seroussi, H., Larour, E., and Rignot, E.: Inversion of Basal Friction in Antarctica Using Exact and Incomplete Adjoints of a Higher-Order Model, Journal of Geophysical Research, 118, 1746–1753, https://doi.org/10.1002/jgrf.20125, 2013.

Morlighem, M., Rignot, E., Binder, T., Blankenship, D., Drews, R., Eagles, G., Eisen, O., Ferraccioli, F., Forsberg, R., Fretwell, P., et al.:
500   Deep Glacial Troughs and Stabilizing Ridges Unveiled beneath the Margins of the Antarctic Ice Sheet, Nature Geoscience, 13, 132–137, https://doi.org/10.1038/s41561-019-0510-8, 2020.

Nienow, P. W., Sole, A. J., Slater, D. A., and Cowton, T. R.: Recent Advances in Our Understanding of the Role of Meltwater in the Greenland Ice Sheet System, Current Climate Change Reports, 3, 330–344, https://doi.org/10.1007/s40641-017-0083-9, 2017.

Rignot, E.: MEaSUREs InSAR-Based Antarctica Ice Velocity Map, Version 2, https://doi.org/10.5067/D7GK8F5J8M8R, 2017.

505   Rignot, E., Mouginot, J., and Scheuchl, B.: Ice Flow of the Antarctic Ice Sheet, Science, 333, 1427–1430, https://doi.org/10.1126/science.1208336, 2011.

Schoof, C.: The Effect of Cavitation on Glacier Sliding, Proceedings of the Royal Society A, 461, 609–627, https://doi.org/10.1098/rspa.2004.1350, 2005.

Schoof, C.: Ice Sheet Grounding Line Dynamics: Steady States, Stability, and Hysteresis, Journal of Geophysical Research, 112, 1–19,
510   https://doi.org/10.1029/2006JF000664, 2007.

Schroeder, D. M., Blankenship, D. D., and Young, D. A.: Evidence for a Water System Transition beneath Thwaites Glacier, West Antarctica, Proceedings of the National Academy of Sciences, 110, 12 225–12 228, https://doi.org/10.1073/pnas.1302828110, 2013.

Sergienko, O. V., Creyts, T. T., and Hindmarsh, R. C. A.: Similarity of Organized Patterns in Driving and Basal Stresses of Antarctic and Greenland Ice Sheets beneath Extensive Areas of Basal Sliding, Geophysical Research Letters, 41, 3925–3932,

515   https://doi.org/10.1002/2014gl059976, 2014.

Seroussi, H., Nowicki, S., Simon, E., Abe-Ouchi, A., Albrecht, T., Brondex, J., Cornford, S., Dumas, C., Gillet-Chaulet, F., Goelzer, H., Golledge, N. R., Gregory, J. M., Greve, R., Hoffman, M. J., Humbert, A., Huybrechts, P., Kleiner, T., Larour, E., Leguy, G., Lipscomb, W. H., Lowry, D., Mengel, M., Morlighem, M., Pattyn, F., Payne, A. J., Pollard, D., Price, S. F., Quiquet, A., Reerink, T. J., Reese, R., Rodehacke, C. B., Schlegel, N.-J., Shepherd, A., Sun, S., Sutter, J., Van Breedam, J., van de Wal, R. S. W., Winkelmann, R., and Zhang, T.:

520   initMIP-Antarctica: An Ice Sheet Model Initialization Experiment of ISMIP6, The Cryosphere, 13, 1441–1471, https://doi.org/10.5194/tc-13-1441-2019, 2019.

van der Veen, C. J.: Longitudinal Stresses and Basal Sliding: A Comparative Study, in: Dynamics of the West Antarctic Ice Sheet, edited by Van der Veen, C. J. and Oerlemans, J., Glaciology and Quaternary Geology, pp. 223–248, Springer Netherlands, Dordrecht, https://doi.org/10.1007/978-94-009-3745-1_13, 1987.

525   van Wessem, J. M., Van De Berg, W. J., Noël, B. P. Y., Van Meijgaard, E., Amory, C., Birnbaum, G., Jakobs, C. L., Krüger, K., Lenaerts, J., Lhermitte, S., Ligtenberg, S. R. M., Medley, B., Reijmer, C. H., van Tricht, K., Trusel, L. D., van Ulft, L. H., Wouters, B., Wuite, J., and van den Broeke, M. R.: Modelling the Climate and Surface Mass Balance of Polar Ice Sheets Using RACMO2: Part 2: Antarctica (1979-2016), The Cryosphere, 12, 1479–1498, https://doi.org/10.5194/tc-12-1479-2018, 2018.

Weertman, J.: On the Sliding of Glaciers, Journal of Glaciology, 3, 33–38, 1957.

530   Werder, M. A., Hewitt, I. J., Schoof, C. G., and Flowers, G. E.: Modeling Channelized and Distributed Subglacial Drainage in Two Dimensions, Journal of Geophysical Research, 118, 1–19, https://doi.org/doi:10.1002/jgrf.20146,, 2013.

Winkelmann, R., Martin, M. A., Haseloff, M., Albrecht, T., Bueler, E., Khroulev, C., and Levermann, A.: The Potsdam Parallel Ice Sheet Model (PISM-PIK) - Part 1: Model Description, The Cryosphere, 5, 715–726, https://doi.org/10.5194/tc-5-715-2011, 2011.

Yu, H., Rignot, E., Seroussi, H., and Morlighem, M.: Retreat of Thwaites Glacier, West Antarctica, over the next 100 Years Using Various

535   Ice Flow Models, Ice Shelf Melt Scenarios and Basal Friction Laws, The Cryosphere, 12, 3861–3876, 2018.